Fluid Phase Equilibria 498 (2019) 72–85

Contents lists available at ScienceDirect

Fluid Phase Equilibria

journal homepage: www.elsevier.com/locate/fluid

A novel pore-size-dependent equation of state for modeling fluid phase behavior in nanopores

Sheng Luo [a], Bikai Jin [a], Jodie L. Lutkenhaus [b, c, **], Hadi Nasrabadi [c, *]

[a] Harold Vance Department of Petroleum Engineering, Texas A&M University, College Station, TX, 77843, USA
[b] Artie McFerrin Department of Chemical Engineering, Texas A&M University, College Station, TX, 77843, USA
[c] Department of Materials Science and Engineering, Texas A&M University, College Station, TX, 77843, USA

ARTICLE INFO

Article history:
Received 8 October 2018
Received in revised form
23 May 2019
Accepted 10 June 2019
Available online 13 June 2019

Keywords:
Equation of state
Confined fluid
Phase equilibrium
Adsorption
Differential scanning calorimetry

ABSTRACT

The thermodynamic behavior of fluids confined in nanopores differs from that of bulk fluid by the fluid-pore wall interaction. Inspired by the heterogeneous distribution and layering transitions from fluid-wall interactions, we have developed a pore-size-dependent equation of state (EOS) extended from the Peng-Robinson equation of state (PR EOS) by describing the confined fluid as distinct populations of surface-adsorbed and core fluid. The surface-adsorbed fluid physically corresponds to two surface-adsorbed layers and is therefore considered to interact with the pore wall through a dual-square-well (DSW) potential function. The presented EOS requires only one additional parameter of confinement energy (ε_{sf}) beyond PR EOS, and it needs to be determined from experimental data. Using adsorption and differential scanning calorimetry experiments, we determine the confinement parameter ε_{sf} for nitrogen, carbon dioxide, *n*-alkanes of methane to *n*-tetradecane, with respect to surfaces of native silica and silylated silica. The resulting database of confinement parameters is presented. This EOS models adsorption isotherms, phase transition temperature, and phase transition-pore size relations, in agreement with experimental data. The EOS is shown to be a unified tool for modeling the fluid phase behavior in nanopores.

1. Introduction

Due to the fluid-pore wall interaction in the confining geometry, the thermodynamics and kinetics of confined fluid significantly differ from the bulk state. The phase behavior of fluid in confined space is essential in many industrial applications, such as pollution control [1], drug delivery [2], catalyst design [3], and oil and gas production [4]. For fluid applications in complex nanoporous system, a proper approach to model the confined phase behavior is highly desired. For example, in oil and gas recovery from unconventional shale resources where the nanopores are abundant, the phase behavior of nano-confined fluid is crucial in assessing hydrocarbon in-place [5] and predicting well performance [4].

Experimentally, fluid phase behavior in nanopores has been widely studied through isothermal physisorption, for fluids such as argon [6], nitrogen [7], light and intermediate hydrocarbons [8,9]. Recently, Luo et al. developed an isobaric measurement of phase transition temperature for confined hydrocarbons using differential scanning calorimetry (DSC) and various intermediate to heavy hydrocarbons in different sizes of nanopores were studied [10–12]. Theoretically, the fluid phase behavior in nanopores is governed by the interactions of fluid-fluid and fluid-pore wall interactions within the confining geometry. Since the fluid-fluid interaction is defined with the bulk-state thermodynamics, an additional definition of fluid-pore wall interaction along with the pore geometry completes the thermodynamics system. Based on that, the molecule-level approaches, such as molecular simulation [13–16] and density functional theory [17,18] (DFT), are applied in studying the confined fluid, and useful insight are obtained into the fluid structures and phase transition mechanisms. Using grand canonical Monte Carlo molecular simulation with Lennard-Jones potential, Walton and Quirke obtained good correlations with experiments and showed that capillary condensation occurs as a density jump from a low, vapor-like state to a high, liquid-like state, and that the vapor-like state consists of surface-adsorbed layers and a low-density core [13]. Li et al. found the layering transitions of the adsorbed phases prior to capillary condensation for short Lennard-

* Corresponding author.
** Corresponding author. Artie McFerrin Department of Chemical Engineering, Texas A&M University, College Station, TX, 77843, USA.
E-mail addresses: jodie.lutkenhaus@tamu.edu (J.L. Lutkenhaus), hadi.nasrabadi@tamu.edu (H. Nasrabadi).

https://doi.org/10.1016/j.fluid.2019.06.009
0378-3812/

Jones chain molecules, and that the critical temperature of condensation/evaporation is lower than that of the bulk fluid [19]. Recently, Zhang et al. applied multi-square-well (MSW) potential in DFT and the multi-layering mechanism in the adsorptions by nanopores is demonstrated [20,21].

The equation of state (EOS) is one of the most used and studied approaches in thermodynamic modeling and it has accomplished tremendous success in modeling bulk-state fluid behavior [22,23]. To model the confined fluid behavior, the EOS system requires the description of fluid-pore wall interaction, which is generally implemented by two approaches: one is to define it as capillary effect, which is quantified as a pressure difference between the vapor and liquid phase (capillary pressure); the other is to directly describe the fluid-pore wall interaction as a force field. The capillary pressure utilizes the Young-Laplace equation, which assumes a smooth and homogeneous liquid/vapor interface and bulk-state surface tension. This approach yields the Kelvin equation, and it is recently used in various studies coupled with the Peng-Robinson equation of state (PR EOS) [24–27] and perturbed-chain statistical associating fluid theory (PC-SAFT) [28,29]. For the approach of directly describing the force field, Travalloni et al. extended the cubic EOS to cylindrical nanopores based on generalized van der Waals theory by defining the fluid-pore wall interaction as a single square-well potential and the resulting Peng-Robinson-Confined equation of state (PR-C EOS) is applied in modeling adsorptions in nanoporous media [30,31]. Later, Travalloni et al. reformulated the extended EOS based on molecular simulations [32], and most recently, new mixing rules and an extension to spherical pores are reported [33]. PR-C EOS requires two parameters of square-well depth and width, which need to be determined from experiments. Elsewhere, Dong et al. applied the multicomponent potential theory of adsorption (MTPA) with PR EOS modeling [34], and Dawass et al. used external fields in calculating the spatial segregation of confined components [35].

The direct description of fluid-pore wall interaction of PR-C EOS is physically consistent with the molecule-level simulations such as molecular simulation and DFT. However, PR-C EOS uses single-square-well (SSW) potential for the fluid-wall interaction [31,36] to describe one layer of adsorbed fluid. PR-C EOS does not distinguish between the fluid on the surface and the fluid in the center, and it does not properly model the multi-layered fluid properties and layering transitions [19,37] from experiments. A sophisticated model with the consideration of multi-layering is required to yield a general EOS modeling in correlation with experimental results under various conditions.

In this work, we model the confined fluid as two distinct populations of surface-adsorbed and core fluid and apply a dual-square-well (DSW) potential for fluid-wall interaction. The surface-adsorbed fluid consists of two molecular layers. Guided by the generalized van der Waals theory, a pore-size-dependent equation of state is extended from PR EOS based on molecular simulations. The resulting EOS requires only one additional parameter of confinement energy beyond PR EOS. The confinement parameter is determined for various species and the general applicability of the EOS is studied.

2. Formulation of equation of state

2.1. Fluid model

Herein, we formulate a pore-size-dependent equation of state extended from the Peng-Robinson equation of state by the generalized van der Waals theory. For a system with given numbers of molecules (N_1, N_2, …, N_{NC}), volume (V) and temperature (T), the thermodynamic properties can be derived from the generalized van der Waals canonical partition function (Q) [30,38]:

$$Q(T,V,N_1,N_2,\ldots,N_{Nc}) = \prod_{i=1}^{NC}\left(\frac{q_i^{N_i}}{\lambda_i^{3N_i}N_i!}\right)V_f^N \exp\left(\int_\infty^T \frac{E_{conf}}{k_B T^2}dT\right) \tag{1}$$

The Helmholtz free energy (A), chemical potential (μ) and pressure (P) are derived as:

$$A(T,V,N_1,N_2,\ldots,N_{Nc}) = -kT\ln Q(T,V,N_1,N_2,\ldots,N_{NC}) \tag{2}$$

$$\mu_i = \left(\frac{\partial A}{\partial N_i}\right)_{T,V,N_{j\neq i}} \tag{3}$$

$$P = -\left(\frac{\partial A}{\partial V}\right)_{T,N_1,N_2,\ldots,N_{NC}} \tag{4}$$

The fluid model in nanopores is framed based on the fluid distributions. As commonly observed in adsorptions by nanopores, multi-layers of fluid are adsorbed onto the pore wall before pore condensation takes place [19]. For example, in the study of capillary condensation for argon, Wongkoblap et al. found a two-step pore filling processes as a first adsorption of two layers on surface followed by four layers packed in the center [37]. By Monte Carlo molecular simulations, we observed that: initially one layer of fluid is adsorbed on to the pore wall, Fig. 1A; next, another layer of molecules are adsorbed and the thickness of each layer is σ, Fig. 1B; then, pore filling leads to phase transition in the center of the pore and the pore is fully filled, Fig. 1C; further pore filling results in the nanopore densely packed with fluid, Fig. 1D. Based on such observations, we consider two-molecular layers of surface-adsorbed fluid. The total fluid in a nanopore is considered as two distinct populations (Fig. 1): one is the bulk-like core fluid beyond the attraction of the wall (Region I), the other is the surface-adsorbed fluid which interacts with pore wall (Region II) [36,39]. The Helmholtz free energy of the fluid in the nanopore is the sum of surface-adsorbed and core fluid, Eq. (5).

$$A = A_{co} + A_{sf} \tag{5}$$

Multiple-square-well (MSW) potential is a useful method in describing the fluid-wall interactions and it effectively models the layering mechanisms by discretizing attractive force fields with respect to distance from the wall [21,40]. In this work, a dual-square-well (DSW) potential is used to describe the fluid-pore wall interaction by the distance from the wall, shown in Eq. (6). The first square well has a depth ε_{sf} and the second well's depth is $\frac{1}{4}\varepsilon_{sf}$. Each square well has a width of σ (Fig. 2) and σ is the molecular diameter. This potential function specifically describe the interaction of fluid in Region II with pore wall, where the first square well (ε_{sf}) denotes the interaction for layer 1 and the second square well ($\frac{1}{4}\varepsilon_{sf}$) denotes the interaction for layer 2.

$$u_{sf,i}(r) = \begin{cases} \infty & r < 0.5\sigma_i \\ -\varepsilon_{sf,i} & 0.5\sigma_i < r < 1.5\sigma_i \\ -\frac{1}{4}\varepsilon_{sf,i} & 1.5\sigma_i < r < 2.5\sigma_i \\ 0 & 2.5\sigma_i < r \end{cases} \tag{6}$$

The equation of state is extended from PR EOS: the energy

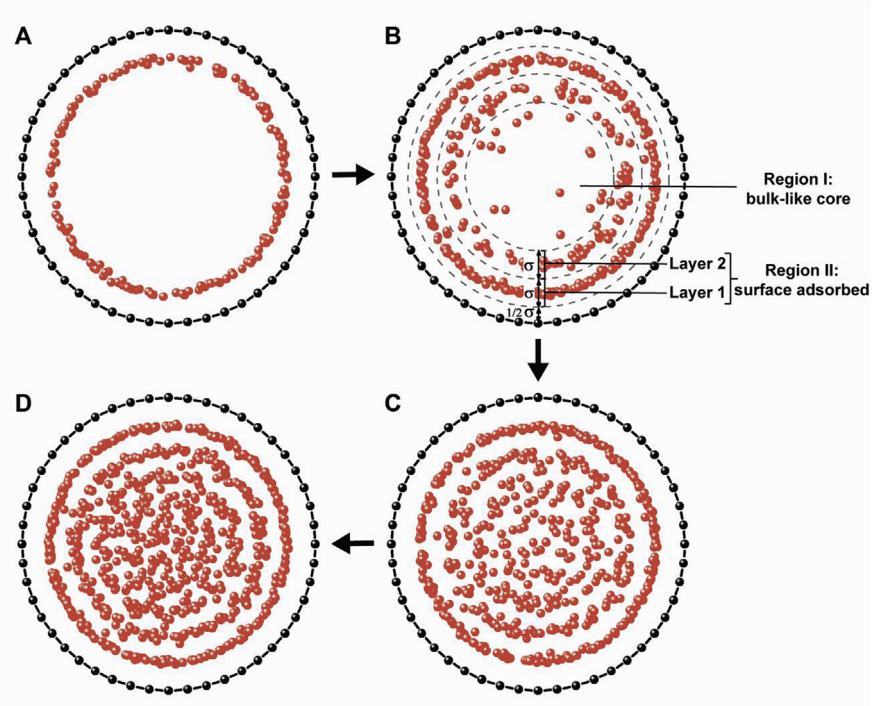

Fig. 1. Snapshots of methane filling the nanotube ($r_p/\sigma = 5.0$). A: one adsorbed layer; B: two adsorbed layers; C: fully-filled pore (after phase transition); D: pore filled with fluid at high density. Two regions of fluid in nanopore: bulk-like core region and surface-adsorbed region. The surface-adsorbed fluid consists of two layers of molecules with each layer of thickness σ. The bulk-like core fluid relates to those in the center.

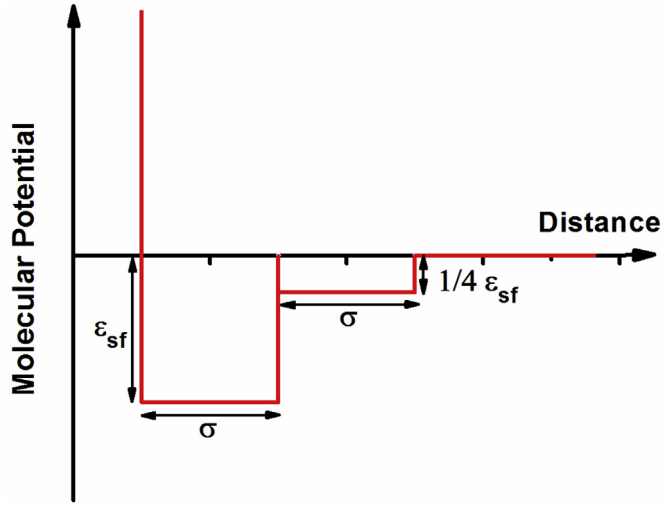

Fig. 2. Dual-square-well potential for fluid-pore wall interaction: the first and second square wells correspond to the interactions with layer 1 and 2, respectively, in Region II.

parameter (a) and volume parameter (b) of the conventional PR EOS [22] are used in this new EOS. Based on the generalized van der Waals theory, PR EOS agrees to a square-well potential system, Eq. (7), and implies the fluid molecule-molecule interaction (ε_{ff}) as Eq. (8) [31,41], where $\rho_{\max,i}$ is the close-packing molecular density for component i and R_{sw} is the range of the square well.

$$u_{ii}(r) = \begin{cases} \infty & r < \sigma_i \\ -\varepsilon_{ff,ii} & \sigma_i < r < R_{sw}\sigma_i \\ 0 & r > R_{sw}\sigma_i \end{cases} \tag{7}$$

$$\varepsilon_{ff,ii} = \frac{a\rho_{max,i}}{\sqrt{2}N_{av}^2\alpha_{PR}} \tag{8}$$

2.2. Free volume

Consistent with the cubic equation of state, the free volume (V_f) in Eq. (1) is modeled as:

$$V_f = V - \sum_{i=1}^{NC}\left(\frac{N_i}{\rho_{max,i}}\right) \tag{9}$$

Using the packing data, Travalloni et al. reported a correlation of close-packing molecular density ($\rho_{\max,i}$) with pore radius (r_p) and molecular diameter (σ) for fluid in cylindrical pores [30,31]:

$$\rho_{max,i}\sigma_i^3 = 1.158 - 0.479\exp\left(0.621\left(0.5 - \frac{r_p}{\sigma_i}\right)\right) + 0.595\exp\left(4.014\left(0.5 - \frac{r_p}{\sigma_i}\right)\right) \tag{10}$$

The close-packing molecular density is considered the same for core ($\rho_{\max,co,i}$) and surface-adsorbed regions ($\rho_{\max,sf,i}$), and both are equal to $\rho_{\max,i}$. In agreement with volume formulation in PR EOS, molecular diameter (σ) is defined as [41]:

$$\sigma_i = \sqrt[3]{\frac{1.158b_i}{N_{av}}} \tag{11}$$

2.3. Configurational energy

Assuming the pairwise interactions of fluid molecule-molecule interaction and fluid molecule-pore wall interactions by the square-wells described in Eqs. (6) and (7), the configurational energy (E^{conf}) for core and surface-adsorbed fluid are:

$$E_{co}^{conf} = -\sum_{i=1}^{NC}\sum_{j=1}^{NC}\left(\frac{N_{co,j}}{2}N_{c,co,ij}\varepsilon_{ff,ij}\right) \tag{12}$$

$$E_{sf}^{conf} = -\sum_{i=1}^{NC}\sum_{j=1}^{NC}\left(\frac{N_{sf,j}}{2}N_{c,sf,ij}\varepsilon_{ff,ij}\right) - \sum_{i=1}^{NC}\left(N_{layer\ 1,i}\varepsilon_{sf,i}\right) - \sum_{i=1}^{NC}\left(\frac{1}{4}N_{layer\ 2,i}\varepsilon_{sf,i}\right) \tag{13}$$

We define that F_{p1} represents the fraction of the fluid in the first layer, and F_{p2} represents the fraction for the sum of fluid in the first and second layers. Number of the molecules in core region (N_{co}) and surface-adsorbed region (N_{sf}), as well as the first ($N_{layer\ 1}$) and the second layer ($N_{layer\ 2}$), are related to the total number of molecules in pore (N) as:

$$N_{co,i} = N_i(1 - F_{p2,i}) \tag{14}$$

$$N_{sf,i} = N_i F_{p2,i} \tag{15}$$

$$N_{layer\ 1,i} = N_i F_{p1,i} \tag{16}$$

$$N_{layer\ 2,i} = N_i(F_{p2,i} - F_{p1,i}) \tag{17}$$

Next, Monte Carlo simulations based on canonical ensemble is conducted to obtain the molecular distributions in nanopores. In the canonical ensemble, the number of particles, temperature and volume are constant (*NVT*-constant). Methane is used as the model species and the graphite nanotube is applied as the pore wall. The particles interact through the Lennard-Jones potential [15]. The nanotube is designed with the height of 42.54 Å with different diameters. Periodic boundary condition is only applied in the axial direction. At each temperature, a series of simulations are performed by varying the molecular number. After 6 million Monte Carlo steps, the system snapshots of molecule distributions are generated per 10000 steps in the last 1 million moves.

We use the functions which employs a Gaussian-like part with exponent parameter γ to correlate the molecular distribution of layer one (F_{p1}) and two layers (F_{p2}) to the total fluid density in pore (ρ/ρ_{max}), shown in Eqs. (18) and (19).

$$F_{p1} = F_{pr1} + (1 - F_{pr1})\left(1 - \exp\left(-\frac{\beta_o}{T}\right)\right)\left(1 - \exp\left(-\beta_1\left(\frac{\rho_{max}}{\rho} - 1\right)^{\gamma}\right)\right) \tag{18}$$

$$F_{p2} = F_{pr2} + (1 - F_{pr2})\left(1 - \exp\left(-\frac{\beta_o}{T}\right)\right)\left(1 - \exp\left(-\beta_2\left(\frac{\rho_{max}}{\rho} - 1\right)^{\gamma}\right)\right) \tag{19}$$

The random distribution fractions (F_{pr1} and F_{pr2}) use the forms:

$$F_{pr1} = \frac{(r_p - 0.5\sigma)^2 - (r_p - 1.5\sigma)^2}{(r_p - 0.5\sigma)^2} \cdot \exp\left(-\frac{\tau_1}{\left(\frac{r_p}{\sigma} - 0.5\right)^{\tau_2}}\right) \tag{20}$$

$$F_{pr2} = \frac{(r_p - 0.5\sigma)^2 - (r_p - 2.5\sigma)^2}{(r_p - 0.5\sigma)^2} \cdot \exp\left(-\frac{\tau_1}{\left(\frac{r_p}{\sigma} - 0.5\right)^{\tau_2}}\right) \tag{21}$$

where τ_1 and τ_2 are universal parameters for random distribution fractions. The parameters β_0, β_1 and β_2 are defined as:

$$\beta_0 = s_1 T_C \left(\frac{\varepsilon_{ff}}{\varepsilon_{sf}}\right)^{s_2} \tag{22}$$

$$\beta_1 = \frac{s_3}{\left(\frac{r_p}{\sigma} - 0.5\right)^{s_5}} \tag{23}$$

$$\beta_2 = \frac{s_4}{\left(\frac{r_p}{\sigma} - 0.5\right)^{s_5}} \tag{24}$$

The F_{p1} and F_{p2} functions are fitted against simulated distributions with varying pore radius (r_p/σ), fluid-pore wall interaction strength ($\varepsilon_{sf}/\varepsilon_{ff}$) and reduced temperature (T_r, i.e. T/T_C). The values of universal parameters of γ, $\tau_{1\text{-}2}$ and $s_{1\text{-}5}$ are listed in Table 1. The fitting results are plotted in Figs. 3 and 4. Generally, F_{p1} approaches the random distribution value of F_{pr1} when $\rho/\rho_{max} \to 1$, as the pore gets fully packed; as ρ/ρ_{max} decreases, F_{p1} greatly increases, because pore evaporation takes place in the center of the pore but the surface-region is still populated with adsorbed molecules; when $\rho/\rho_{max} \to 0$, F_{p1} reaches a plateau as most fluid are adsorbed on the pore wall. As pore radius increases, the plateau shrinks and the mass fraction of surface-adsorbed fluid becomes minor with respect to the total fluid (Fig. 3a). At $r_p/\sigma = 53.6$, the bulk-like core region dominates: for a broad range of density, F_{p1} is close to the baseline of random distribution value. The behavior of two-layer fraction function (F_{p2}) is similar to that of single layer (F_{p1}) (Fig. 3b). Fig. 4a shows that a weaker fluid-pore surface interaction ($\varepsilon_{sf}/\varepsilon_{ff}$) results in a narrower plateau at low density as the weaker force field attracts less fluid molecules in the surface layers. By increasing the temperature (T_r), the plateau shifts downward, which can be explained as higher temperature increases the random thermal motion and the molecules are prone to distribute randomly in the pore (Fig. 4b). These observations are in agreement with the findings in previous studies [30,32].

2.4. Coordination number

Coordination number (N_c) is the number of molecules around a central molecule. Guided by the generalized van der Waals theory, the bulk fluid model in PR EOS adopts the coordination number ($N_{c,b}$) with the form Eq. (25) [42], where $g(T)$ is a function related to the temperature dependency of energy [32].

Table 1
Summary of universal parameters for Eqs. 18–24 and coordination number coefficient.

γ	τ_1	τ_2	s_1	s_2	s_3	s_4	s_5	h_{sf}
1.6784	0.4698	0.2322	4.2801	1.8191	1.9417	4.5587	1.4942	0.8989

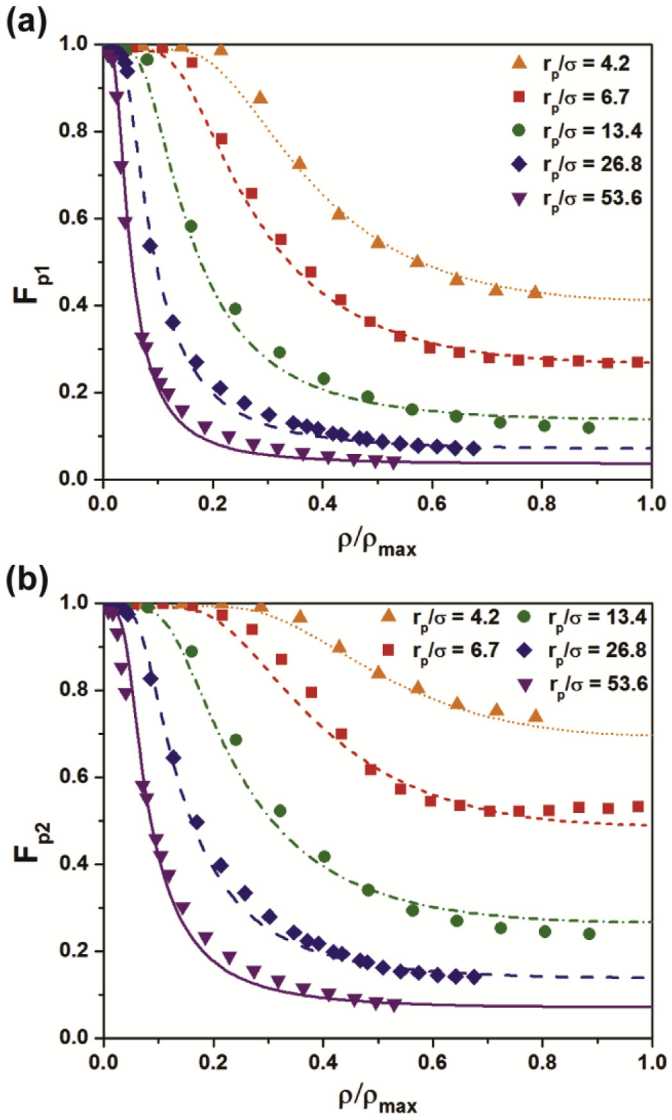

Fig. 3. Surface-adsorbed fluid fraction data from molecular simulations (symbols) and fitting results (lines) at different pore radii: (a) the first layer (b) sum of the first and second layer (two layers). The temperature (T_r) is 0.79 and the fluid-wall interaction energy ($\varepsilon_{sf}/\varepsilon_{ff}$) is 0.45.

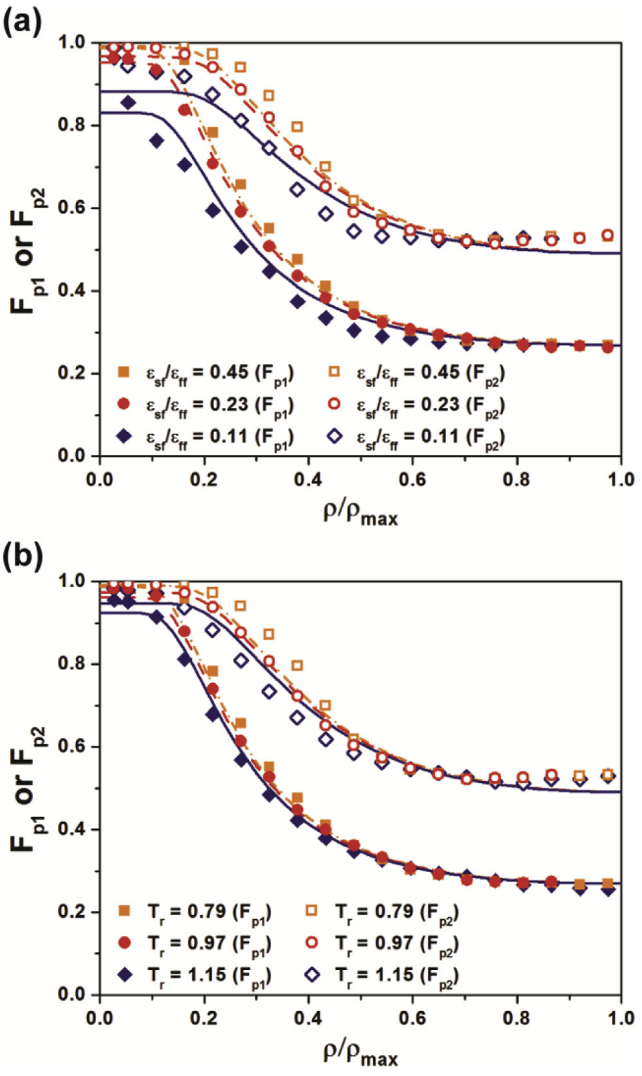

Fig. 4. Surface-adsorbed fluid fraction data from molecular simulations (symbols) and fitting results (lines) as a function of: (a) fluid-wall interaction energy ($\varepsilon_{sf}/\varepsilon_{ff}$) with $T_r = 0.79$ (b) temperature (T_r) with $\varepsilon_{sf}/\varepsilon_{ff} = 0.45$. In both scenarios, $r_p/\sigma = 6.7$.

$$N_{c,b} = g(T)\ln\left(\frac{1+\left(1+\sqrt{2}\right)\rho/\rho_{max}}{1+\left(1-\sqrt{2}\right)\rho/\rho_{max}}\right) \tag{25}$$

$$N_{c,sf} = h_{sf}N_{c,b} \tag{26}$$

Due to the steric hindrance of the pore wall, the surface-adsorbed-region fluid generally has a smaller coordination number than the bulk-state fluid. As shown in Fig. 5, the coordination of surface-adsorbed fluid is approximately independent from pore radius, as the fluid distribution is dominated by the two-dimensional layering on the pore wall. By fitting the coordinate number of surface fluid in linear relation to that of bulk fluid, we obtained the coefficient h_{sf} as 0.8989, Eq. (26). Since the core fluid are located beyond the pore wall force field and behaves in a three-dimensional fashion, the core fluid coordination number ($N_{c,co}$) is taken the same as bulk coordinate number ($N_{c,b}$). Herein, the universal fitting parameters are summarized in Table 1.

2.5. Equation of state

As is generally used in PR EOS [43], the volume translation is applied to relate experimental total pore volume to the EOS volume:

$$v = v^{CORR} + \sum_{i=1}^{NC} x_i c_i \tag{27}$$

As the surface-adsorbed fluid is defined to be the first two layers of fluid, the volume of surface-region fluid (V_{sf}) is related to the total volume of fluid (V), Eq. (28). The volume of core fluid is written as Eq. (29), accordingly. $\overline{F}_{pr2}$ is the surface-adsorbed layer fraction, weighted by the components' fractions (x_i) in the total system, Eq. (30). Eqs. 18–24 are used in calculating $F_{pr1,i}$ and $F_{pr2,i}$ for each component i.

$$V_{sf} = V\overline{F}_{pr2} \tag{28}$$

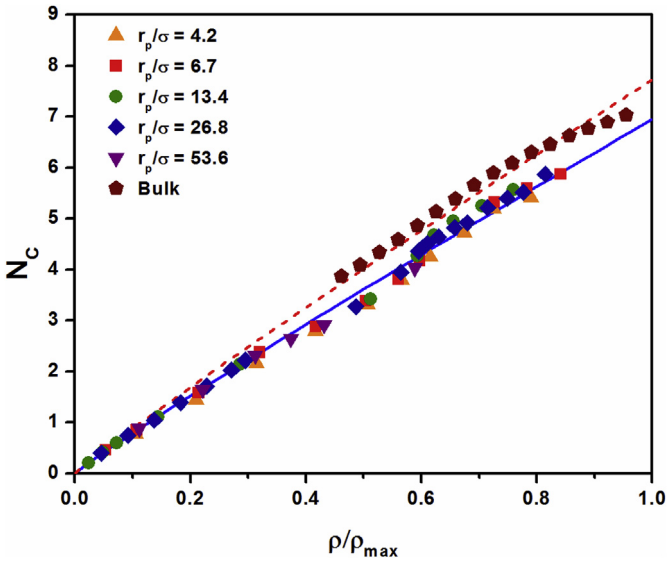

Fig. 5. Surface-adsorbed fluid coordinate numbers from molecular simulations (symbols) and fitting results (lines) at different pore radius ($\varepsilon_{sf}/\varepsilon_{ff} = 0.45$, $T_r = 0.79$).

$$V_{co} = V(1 - \overline{F}_{pr2}) \tag{29}$$

$$\overline{F}_{pr2} = \sum_{i=1}^{NC} x_i F_{pr2,\,i} \tag{30}$$

With the generalized van der Waals partition function Eq. (1) fully described for core fluid and surface-adsorbed fluid, the Helmholtz free energy of each is derived by Eq. (2). The sum of the two regions yields the Helmholtz free energy of the total fluid in pore by Eq. (5).

Herein, we present the complete set of equations. In this EOS, the bulk fluid properties are used and the only extra parameter to be determined from experimental data is the fluid-wall interaction energy parameter (ε_{sf}). The PR EOS parameters are calculated as [22]:

$$m_i = \begin{cases} 0.37464 + 1.54226\omega_i - 0.26992\omega_i^2, & 0 < \omega_i \le 0.5 \\ 0.3796 + 1.485\omega_i - 0.1644\omega_i^2 + 0.01667\omega_i^3, & \omega_i > 0.5 \end{cases} \tag{31}$$

$$a_i = \frac{0.45724 R^2 T_{C,i}^2}{P_{C,i}} \left(1 + m_i \left(1 - \sqrt{\frac{T}{T_{C,i}}}\right)\right)^2 \tag{32}$$

$$b_i = \frac{0.07780 R T_{C,i}}{P_{C,i}} \tag{33}$$

The component packing density ($\rho_{\max,i}$) and molecular diameter (σ_i) of component i are calculated from Eqs. (10) and (11). The confinement-modified volume parameter ($b_{p,i}$) of component i is [36]:

$$b_{p,i} = \frac{N_{av}}{\rho_{max,i}} \tag{34}$$

The confinement modified energy (a_p) and volume parameter (b_p) of fluid mixtures are expressed separately for bulk core Eq. (35) and surface-adsorbed fluid Eq. (36). The regional molar fractions ($x_{co,i}$ and $x_{sf,i}$) are readily calculated from Eqs. (14) and (15). The binary interaction parameter (k_{ij}) is applied following the formulation of PR EOS.

$$\begin{cases} a_{p,co} = \sum_{i=1}^{NC} \sum_{j=1}^{NC} (1 - k_{ij}) x_{co,i} x_{co,j} \sqrt{a_i a_j} \\ b_{p,co} = \sum_{i=1}^{NC} x_{co,i} b_{p,i} \end{cases} \tag{35}$$

$$\begin{cases} a_{p,sf} = \sum_{i=1}^{NC} \sum_{j=1}^{NC} (1 - k_{ij}) x_{sf,i} x_{sf,j} \sqrt{a_i a_j} h_{sf} \\ b_{p,sf} = \sum_{i=1}^{NC} x_{sf,i} b_{p,i} \end{cases} \tag{36}$$

A relative pore fluid density (θ) is defined based on the molar fractions (x_i) of total fluid:

$$\theta = \frac{v}{\sum_{i=1}^{NC} x_i b_{p,i}} \tag{37}$$

The Helmholtz free energy of the confined fluid is written as Eq. (38). Chemical potential (μ) and pressure (P) are derived from Eqs. (3) and (4).

$$\begin{aligned} A = {} & \sum_{i=1}^{NC} n_i (\mu_{0,i} - RT) + \sum_{rgn=co,sf} \left(\sum_{i=1}^{NC} n_{rgn,i} RT \ln\left(\frac{N_{av} x_{rgn,i} \lambda_i^3}{v_{rgn} - b_{p,rgn}}\right) - \frac{\sqrt{2}}{4} \frac{n_{rgn} a_{p,rgn}}{b_{p,rgn}} \ln\left(\frac{v_{rgn} + \left(1 + \sqrt{2}\right) b_{p,rgn}}{v_{rgn} + \left(1 - \sqrt{2}\right) b_{p,rgn}}\right) \right) \\ & - \sum_{i=1}^{NC} \frac{3}{4} N_{av} n_i \varepsilon_{sf,i} \left(F_{pr1,i} + (1 - F_{pr1,i}) \left(1 - \frac{T}{\beta_{0,i}} \left(1 - \exp\left(-\frac{\beta_{0,i}}{T}\right)\right)\right) (1 - \exp(-\beta_{1,i} (\theta - 1)^{\gamma})) \right) \\ & - \sum_{i=1}^{NC} \frac{1}{4} N_{av} n_i \varepsilon_{sf,i} \left(F_{pr2,i} + (1 - F_{pr2,i}) \left(1 - \frac{T}{\beta_{0,i}} \left(1 - \exp\left(-\frac{\beta_{0,i}}{T}\right)\right)\right) (1 - \exp(-\beta_{2,i} (\theta - 1)^{\gamma})) \right) \end{aligned} \tag{38}$$

3. Results and discussion

3.1. Phase transition descriptions

For either isothermal or isobaric phase transitions, the criteria is described as equal chemical potential (Appendix A) between bulk fluid, coexisting confined and vapor, shown in Eqs. (39) and (40) [11]. It should be noted that the pore fluid density (ρ^V and ρ^L) represents the total density based on the total amount of fluid in pore, and the sub-defined core and surface adsorbed fluid density are obtained by Eqs. (14) and (15).

$$\mu^V_{pore}\left(\rho^V, T, r_p, \varepsilon_{sf}\right) = \mu^L_{pore}\left(\rho^L, T, r_p, \varepsilon_{sf}\right) \tag{39}$$

$$\mu^V_{pore}\left(\rho^V, T, r_p, \varepsilon_{sf}\right) = \mu^V_{bulk}(P, T) \tag{40}$$

In the following parts, the fluid-wall interaction energy parameter (ε_{sf}) in the EOS is firstly determined using the experimental data, then the completed EOS is used to predict confined fluid phase behavior under other conditions. Since the square-well depth represents the strength of the interaction between fluid molecule and pore wall, for a specific fluid, the depth (ε_{sf}) only depends on the nature of pore surface. We use experimental data of which the surface nature of nanoporous materials are categorized into two types: native silica and silylated silica. The silylated silica has organic function groups on surface, which renders it oleophilicity (oil-wet) and hydrophobicity (non-water-wet).

3.2. Modeling of adsorption isotherms

From the physisorptions in nanoporous media, the pore condensation/evaporation pressure generally occurs at a lower pressure than the bulk saturation pressure, and the phase change is associated with the transition between liquid and vapor-like state for the fluid in the center of the pore, while the fluid adsorbed on the pore wall remains in the liquid-like density [13,44]. In EOS modelings, the output is the absolute density of confined fluid, but the adsorption experiment gives the excess adsorption data. By Eq. (41), absolute density is related to the excess adsorption amount. In the following discussions, the calculated adsorption density is compared with the experimental data by adsorbed excess amount, in unit of mmol/cm^3. For cases with hysteresis loop, we specifically models the desorption branch because the desorption corresponds to the phase equilibrium state [45], consistent with the phase equilibria calculated from EOS.

$$n^{excess} = n^{absolute} - \rho_{bulk} V_{pore} \tag{41}$$

First, the model is tested against nitrogen and carbon dioxide adsorptions in nanopores. Cao et al. [8] reported nitrogen adsorptions at 77 K in MCM-41 of native silica surface, with the pore diameter of 3.1 nm. Using the nitrogen phase transition pressure of 0.32 (P/P^0), the fluid-wall interaction energy parameter ε_{sf} is obtained as 604 kB from Eqs. (39) and (40). The volume translation parameter (c) is −0.0039 m^3/kmol. Using the EOS with obtained energy parameter, the isotherm is calculated with Eq. (39). A fair correlation between the simulated and experimental data is observed (Fig. 6a). The simulated isotherm matches well for the liquid-like branch ($P/P^0 > 0.32$) and predicts the second phase transition by the surface-adsorbed layers at very low pressures of ca. 0.02 (P/P^0). However, the modeling result under-predicts the slope of vapor-like branch near phase transition point ($P/P^0 \approx 0.2$–0.3), probably due to the desorption of a less-dense fluctuation zone between adsorbed layers and core [46].

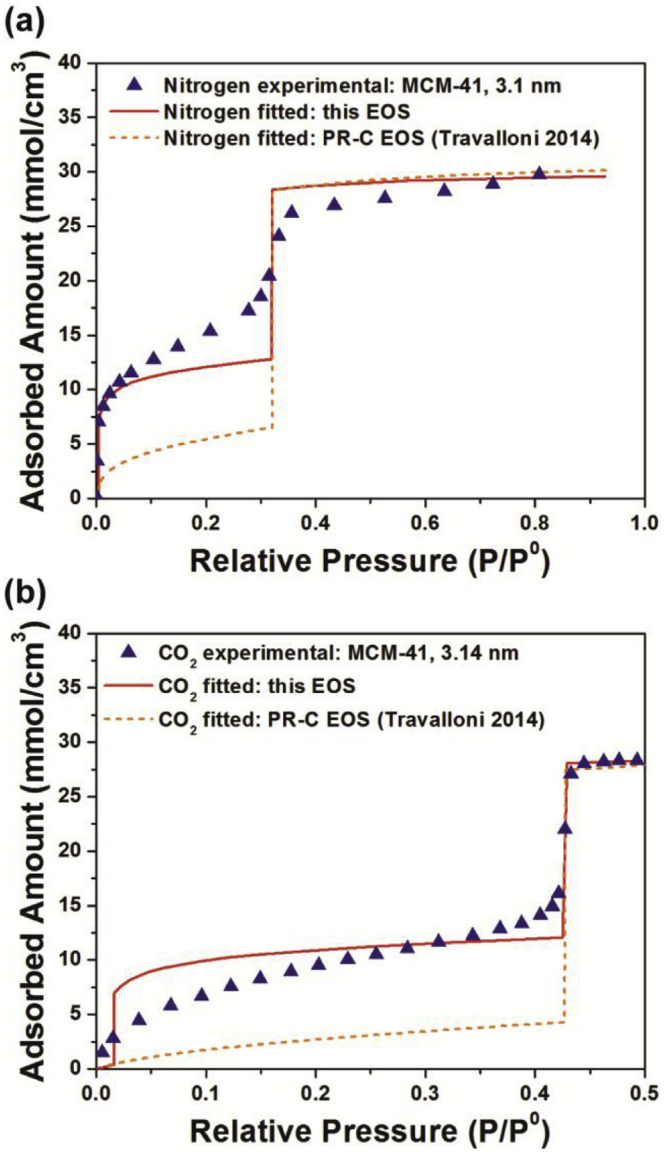

Fig. 6. (a) Nitrogen sorption on MCM-41 (d = 3.1 nm, T = 77 K, native silica surface). (b) Carbon dioxide sorption on MCM-41 (d = 3.1 nm, T = 194.7 K, native silica surface). The symbols represent the experimental data [8,47]. The solid lines are predicted isotherms from this EOS and the dashed lines are the modeling results from PR-C EOS [31].

Modeling the isotherm using the previously reported PR-C EOS [31], the vapor-like branch ($P/P^0 < 0.32$) is significantly under-predicted due to the lack of description for the multi-layer region on surface. Carbon dioxide adsorption in native MCM-41 with 3.1 nm pore diameter [47] is studied, likewise, and ε_{sf} is determined as 1194 kB (volume translation parameter, $c = -0.00078$ m^3/kmol). The proposed EOS with obtained parameter provides a better agreement with the experimental isotherms compared to PR-C EOS (Fig. 6b).

Next, we study the phase transitions and sorption isotherms of hydrocarbons. Emmett and Cines experimentally measured adsorption/desorption of *n*-butane in 3.8 nm Vycor glass [48]. With the experimentally measured phase transition at 0.47 (P/P^0), the confinement parameter is determined as 1641 kB, and the sorption isotherm is simulated with volume translation parameter of −0.0031 m^3/kmol (Fig. 7a). Overall, the EOS simulated isotherm agrees with experimental data, however, the predicted layering

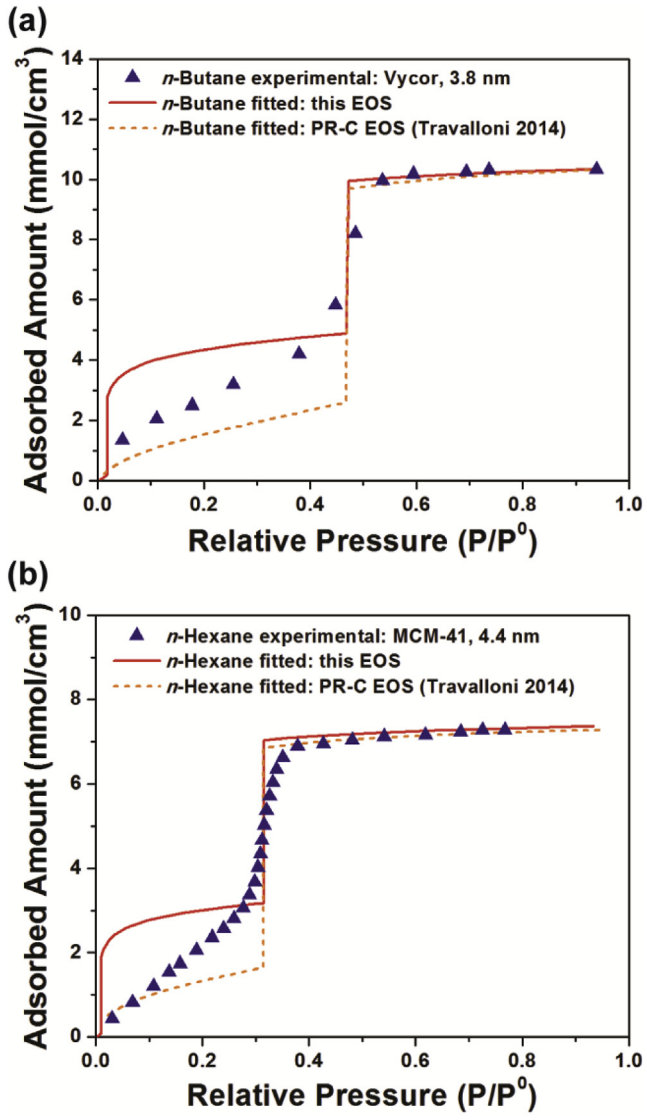

Fig. 7. (a) *n*-Butane sorption in Vycor glass (d = 3.8 nm, T = 273 K, native silica surface) and (b) *n*-hexane sorption in MCM-41 (d = 4.4 nm, T = 313 K, native silica surface). The symbols represent the experimental data [9,48]. The solid line are predicted isotherms from this EOS, and the dashed lines are the modeling results from PR-C EOS [31].

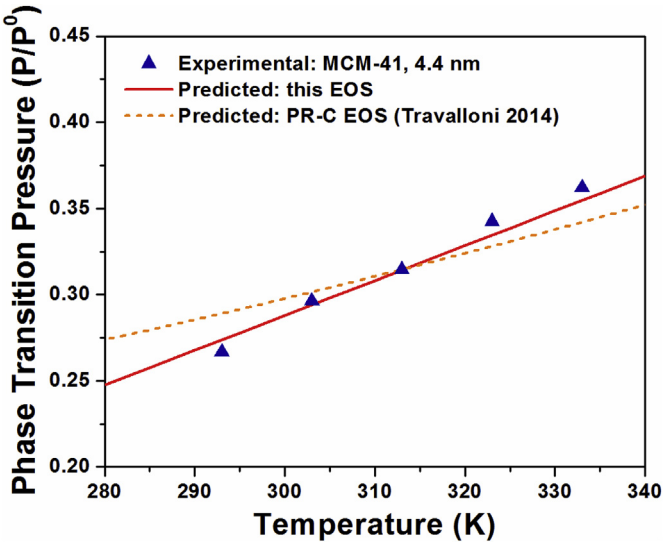

Fig. 8. Temperature dependence of phase transition pressure in MCM-41 (d = 4.4 nm, native silica surface) for *n*-hexane. The symbols represent the experimental data [9]. The solid lines is predicted by this EOS and the dashed line is predicted by PR-C EOS [31].

phase transition at the pressure of 0.03 (P/P^0) is not seen in experimental isotherms. Instead, the experimental isotherm is a smooth ramp of constant slope prior to pore condensation. This could be due to the assumption of smooth walls in the theoretical pore model as it cannot fully reproduce the experimental materials with surface roughness. Tanaka et al. investigated the surface roughness effect on adsorptions using GCMC simulations and found that in the smooth pore model, the isotherm shows a sharp step of layering transition, but with surface roughness isotherm gradually rises with increasing pressure because surface pits disable the build-up of uniform layers [49]. Similar to the case with nitrogen and carbon dioxide, PR-C EOS under-predicts the adsorbed amount prior to pore condensation (Fig. 7a).

Trens et al. studied the confinement effect on adsorption of *n*-hexane at different temperatures [9]. The phase transition pressure of 0.31 (P/P^0) at 313 K in 4.4 nm pore determines the fluid-wall interaction parameter (ε_{sf}) as 2260 kB. Then, the EOS with obtained ε_{sf} is used in predicting the isotherm (c = 0.0019 m^3/kmol). The predictions match part of the experimental isotherm, except the vapor-like branch, likewise in *n*-butane results (Fig. 7b). The EOS predicts phase transition pressures in nanopore and an excellent match is observed against experimental data in the temperature range of 293–333 K (Fig. 8), which shows that this novel EOS is applicable to predicting phase behavior at different temperatures. On the other hand, PR-C EOS under-predicts the temperature-dependence of phase transition pressure.

For the adsorptions without phase transitions, i.e. in supercritical state [50], the energy parameter (ε_{sf}) of fluid-wall interaction is obtained by directly fitting the isotherms. The pore fluid density is calculated from Eq. (42). Fig. 9a and b shows the fittings between the EOS calculated isotherms and the experimental data for methane. The difference of surface nature is reflected in the fluid-pore wall interaction parameter: the parameter ε_{sf} is determined as 664 kB for native silica surface (Figs. 9a) and 411 kB for phenylene-silylated surface (Fig. 9b), respectively. PR-C EOS generally gives similar fitting results.

$$\mu_{pore}\left(\rho_{pore}, T, r_p, \varepsilon_{sf}\right) = \mu^V_{bulk}(P,T) \tag{42}$$

The model is tested for predicting the adsorption of carbon dioxide/ethane binary mixtures on MCM-41 (d = 2.7 nm) [53] using the parameters from fitting the single component experiments. The confinement parameter ε_{sf} for carbon dioxide and ethane are 1194 kB [47] and ε_{sf} 1360 kB [51]. The volume translation parameters of carbon dioxide and ethane are 0.0053 and −0.0121 m^3/kmol. Fig. 10a shows the experimental and modeling results with bulk vapor compositions fixed as $y(CO_2) = 0.1245$. The calculated adsorption isotherms agree well with experimental data at high pressures, while for the low pressure point prior to pore condensation, the adsorbed amount of ethane is overpredicted, similar to the modeling results of single component adsorptions discussed above. Fig. 10b shows the modeled adsorbed amounts under different vapor compositions at constant pressure 1488.28 kPa. Very good agreement is obtained between the experimental data and modeling results. It's worth noting that the adsorbed amount drop at $y(CO_2) = 0.45$ relates to pore evaporation.

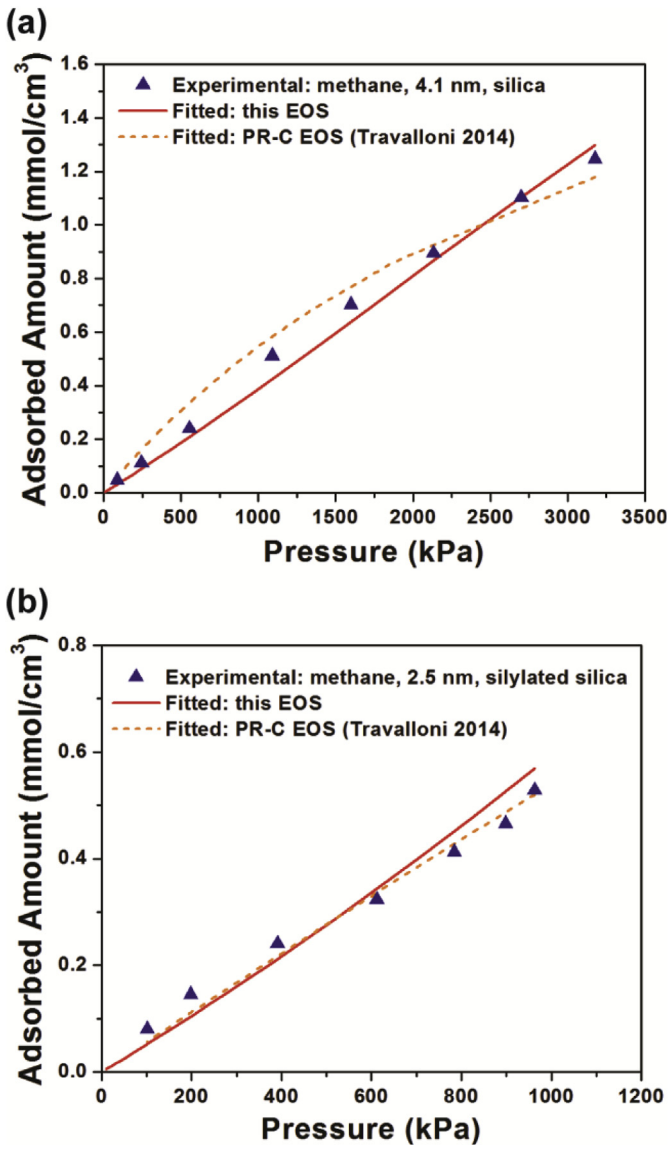

Fig. 9. Adsorption of methane on (a) MCM-41 of native silica surface ($d = 4.1$ nm, $T = 373.2$ K) (b) Ph-PMO of phenylene-silylated silica surface ($d = 2.5$ nm, $T = 298$ K). The symbols represent the experimental data [51,52]. The solid lines are predicted isotherms from this EOS and the dashed lines are the modeling results from PR-C EOS [31].

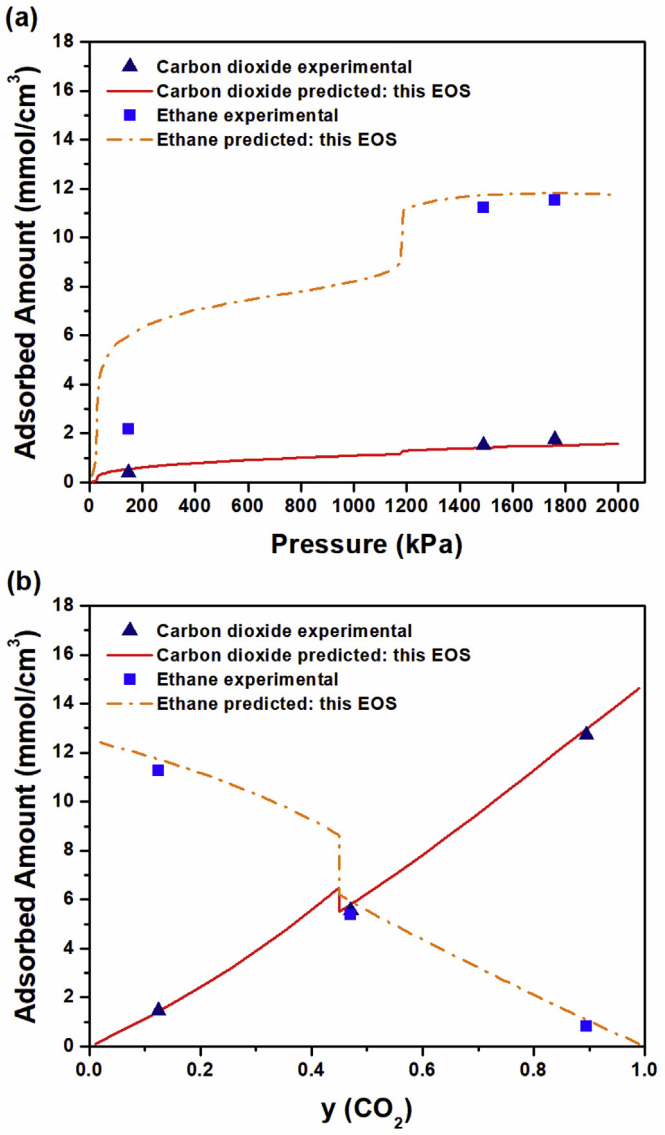

Fig. 10. Adsorption of carbon dioxide/ethane binary mixtures on MCM-41 of native silica surface ($d = 2.7$ nm, $T = 264.6$ K) at (a) constant bulk vapor composition $y(CO_2) = 0.1245$ (b) constant pressure 1488.28 kPa. The symbols represent the experimental data [53]. The lines are predicted from this EOS.

Using the method presented above, the energy parameters ε_{sf} of other species on native silica surface are also obtained from the experimental data. The experimentally fitted parameters ε_{sf} are summarized in Table 2.

3.3. Modeling isobaric phase transitions

An alternative method to assessing the phase transition in nanopore is by changing the temperature at a fixed pressure. Recently, Luo et al. developed the isobaric measurement of phase transition temperature in nanopores using differential scanning calorimetry (DSC) [11,39]. This method has been proved useful in measuring phase transition of hydrocarbons in nanopores, especially for the intermediate to heavy hydrocarbons. In this work, we use DSC to measure the phase transition temperature of *n*-alkanes (*n*-pentane to *n*-tetradecane) in nanopores and apply the phase transition temperatures in determining the energy parameter ε_{sf} for the pore-size-dependent equation of state.

The nanoporous media used in DSC measurement is SBA-16, of which the surface is modified as trimethylsilyl-silica by treatment of hexamethyldisilazane (HMDS). The surface modification renders the porous media oleophilicity and hydrophobicity, and after modification the pore diameter is 6.0 nm. The experimental procedures are found in the previous papers [11,39]. The phase transitions of confined *n*-alkanes (*n*-pentane to *n*-tetradecane) are measured by DSC at atmospheric pressure (101.325 kPa). The thermograms are shown in Fig. 11. Generally, there are two evaporation events: the one at the lower temperature arises from evaporation of the bulk-state fluid outside the nanopores, and the evaporation at the higher temperature is due to the confined fluid evaporations. By measuring the onset of the confined fluid evaporation, the phase transition temperatures are obtained (Table 3). Using the phase transition data, the energy parameter ε_{sf} is solved

Table 2
Energy parameters of fluid-pore wall interaction (ε_{sf}) on native silica surface and experimental source.

Species	ε_{sf} (kB)	Nanoporous Media	Pore Diameter (nm)	Surface	Method	Reference
nitrogen	604	MCM-41	3.1	native silica	isothermal	[8]
carbon dioxide	1194	MCM-41	3.1	native silica	isothermal	[47]
methane	663	MCM-41	4.1	native silica	isothermal	[51]
ethane	1360	MCM-41	4.1	native silica	isothermal	[51]
propane	1421	MCM-41	3.6	native silica	isothermal	[54]
n-butane	1641	Vycor glass	3.8	native silica	isothermal	[48]
n-pentane	2146	MCM-41	4.6	native silica	isothermal	[55]
n-hexane	2260	MCM-41	4.4	native silica	isothermal	[9]

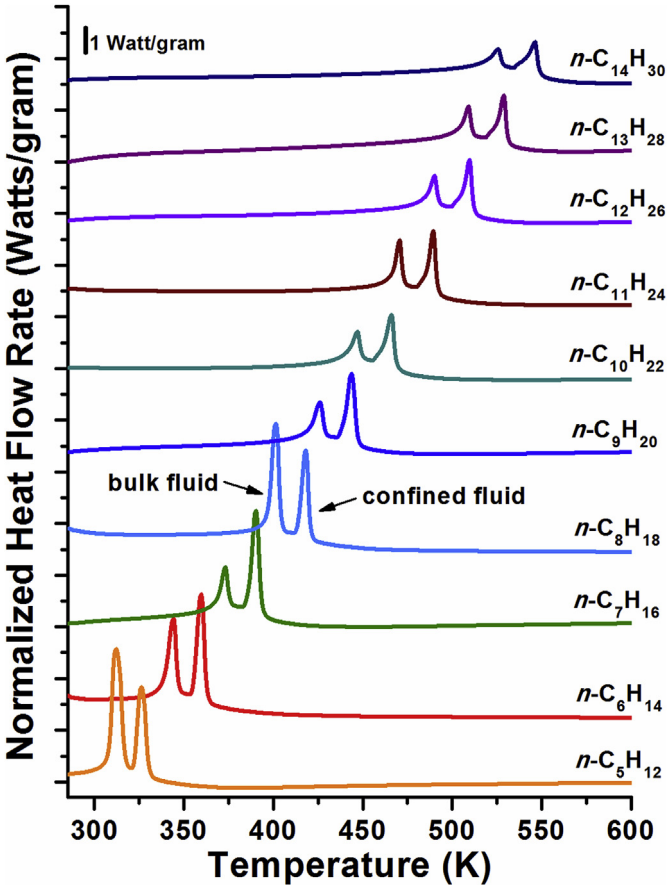

Fig. 11. DSC thermograms of confined *n*-alkanes (*n*-pentane to *n*-tetradecane) at atmospheric pressure (101.325 kPa) in SBA-16 ($d = 6.0$ nm, silylated silica surface). The thermograms of *n*-hexane, *n*-octane and *n*-decane are adopted from the previous paper [11].

Table 3
Phase transition temperature of confined n-alkanes at atmospheric pressure in SBA-16 ($d = 6.0$ nm, silylated silica surface).

Species	T_{sat} (K) at 6.0 nm
n-pentane	322.4
n-hexane	354.8
n-heptane	386.5
n-octane	413.3
n-nonane	438.9
n-decane	463.8
n-undecane	484.9
n-dodecane	504.4
n-tridecane	523.4
n-tetradecane	541.8

for each species by Eqs. (39) and (40). The obtained ε_{sf} values are included in Table 4.

Then we use the EOS to predict phase transitions at different pore sizes. The phase transition temperature-pore diameter relation (Fig. 12, red curve) is calculated using the obtained ε_{sf}. The predictions match experimental results very well [11]: from 50 to 4 nm, the phase transition temperature increases from close to bulk bubble point to 13 K above bulk; further decrease of pore diameter from 4 nm leads to a decrease in phase transition temperature. This novel EOS excellently captures the phase behavior change at ca. 4 nm, which can be attributed to the distinct descriptions of surface-adsorbed and core bulk fluid: as the pore size drops below 4 nm, the fluid behavior cross-overs from the core-fluid dominated to surface-adsorbed-fluid dominated.

Previously, we modeled the phase diagram of *n*-hexane using PR-C EOS [11]. PR-C EOS predicted that fluid is in supercritical state in less than 4 nm pores and the supercritical/subcritical phase boundary is the vertical dashed line (orange) in Fig. 12. It was rationalized that changed phase transition temperature trend at ca. 4 nm is associated with confinement induced supercriticality. On the other hand, our EOS of this work predicts that phase transition temperature decreases as the pore diameter decreases to less than 4 nm, due to the cross-over from core-dominated to surface-dominated phase behavior. In literature, from sorption isochores Thommes and Findenegg observed a decrease of fluid critical temperature in nanopores below the bulk critical temperature [50]. Elsewhere, however, Qiao et al. [56] and Carrott et al. [57] experimentally observed that the phase transitions of *n*-hexane occur in

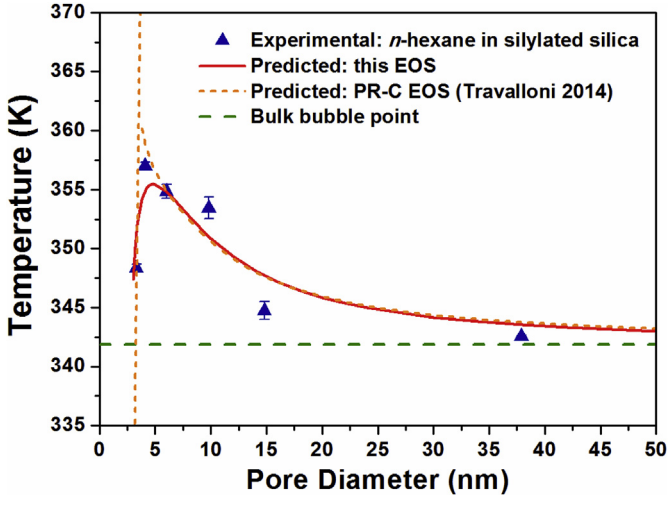

Fig. 12. Experimental and predicted phase transition temperature of *n*-hexane in nanopores of silylated surface. The symbols represents the experimental data [11]. The solid lines are predicted isotherms from this EOS and the dashed lines are the modeling results from PR-C EOS [31].

Table 4
Energy parameters of fluid-pore wall interaction (ε_{sf}) on silylated silica surface.

Species	ε_{sf} (kB)	Nanoporous Media	Pore Diameter (nm)	Surface	Method	Reference
methane	411	Ph-PMO	2.5	phenylene-silica	isothermal	[52]
ethane	678	silica membrane	3.8	trimethylsilyl-silica	isothermal	[59]
propane	1148	silica membrane	3.8	trimethylsilyl-silica	isothermal	[59]
n-butane	1244	silica gel	8.0	dimethyloctadecylsilyl-silica	isothermal	[60]
n-pentane	1593	SBA-16	6.0	trimethylsilyl-silica	isobaric	this work
n-hexane	1621	SBA-16	6.0	trimethylsilyl-silica	isobaric	[11]
n-heptane	1815	SBA-16	6.0	trimethylsilyl-silica	isobaric	this work
n-octane	1883	SBA-16	6.0	trimethylsilyl-silica	isobaric	[11]
n-nonane	1992	SBA-16	6.0	trimethylsilyl-silica	isobaric	this work
n-decane	2131	SBA-16	6.0	trimethylsilyl-silica	isobaric	[11]
n-undecane	2150	SBA-16	6.0	trimethylsilyl-silica	isobaric	this work
n-dodecane	2180	SBA-16	6.0	trimethylsilyl-silica	isobaric	this work
n-tridecane	2244	SBA-16	6.0	trimethylsilyl-silica	isobaric	this work
n-tetradecane	2310	SBA-16	6.0	trimethylsilyl-silica	isobaric	this work

isothermal adsorptions in 3.0–3.8 nm pores. By molecular simulations, Singh showed that in nanopores fluid behavior crossovers from 3D (bulk) to 2D-like in small nanopores and the critical temperature decreases [58]. The detailed mechanism of fluid behavior alternation and the occurrence of phase transition in small nanopores is under further investigation.

At last, we summarize the energy parameters ε_{sf} of species on silylated silica surface fitted from the isobaric experimental data, along with the parameters determined from adsorption isotherms, in Table 4.

4. Conclusion

In this work, a pore-size-dependent equation of state is formulated from the Peng-Robinson equation of state for fluid phase behavior in nanopores. The EOS inherently considers confined fluid as two distinct populations: surface-adsorbed and the bulk-like core fluid. The surface-adsorbed fluid interacts with the pore wall by a dual-square-well (DSW) potential function, while the core fluid separated from the wall's force field. This EOS only requires one confinement parameter of fluid-pore wall interaction energy (ε_{sf}) to be determined from experimental data. We determine the energy parameter (ε_{sf}) for various species on native silica and silylated silica surface with experimental data and the resulting database is presented. The EOS with obtained parameter ε_{sf} decently predicts the adsorption isotherms against experimental measurements. The EOS is applied in predicting phase transition pressure with changed temperature and transition temperatures with changed pore diameters. Both results are in excellent agreement with experimental data. Overall, our EOS is shown as a unified tool for modeling the fluid phase behavior in nanopores.

Acknowledgements

We thank the Crisman Institute at the Petroleum Engineering Department of Texas A&M University for financial support.

Nomenclature

a	energy parameter in the Peng-Robinson equation of state
a_p	energy parameter in the modified Peng-Robinson equation of state
A	Helmholtz free energy
b	volume parameter in the Peng-Robinson equation of state
b_p	volume parameter in the modified Peng-Robinson equation of state
c	volume translation parameter
d	cylindrical pore diameter
E^{conf}	configurational energy
F_{p1}	fraction of fluid molecules in the first adsorbed layer on the pore wall
F_{p2}	fraction of fluid molecules in the first and second adsorbed layers on the pore wall
F_{pr1}	fraction of fluid molecules in the first adsorbed layer on the pore wall under random distribution
F_{pr2}	fraction of fluid molecules in the first and second adsorbed layers on the pore wall under random distribution
h_{sf}	coordination number coefficient for surface-adsorbed fluid
k	binary interaction parameter
k_B	Boltzmann constant
n	moles of fluid molecules
m	Peng-Robinson equation of state parameter for calculating energy parameter
N	number of fluid molecules
N_{av}	Avogadro number
N_c	coordination number
NC	number of components
P	pressure
P_C	critical pressure of bulk-state fluid
P^0	bulk fluid saturation pressure
q	internal partition function
Q	canonical partition function
R	ideal gas constant
r_p	pore radius
$s_{1\text{-}5}$	parameters in fraction functions for surface-adsorbed fluid
T	temperature
T_C	critical temperature of bulk-state fluid
T_r	reduced temperature
u	potential interaction
V	total volume
v	molar volume
x	molar fraction

Greek letters

α_{PR}	function of temperature and acentric factor for the Peng-Robinson equation of state
β	parameters in fraction functions for surface-adsorbed layers

γ	exponent of the Gaussian-like part in fraction functions for surface-adsorbed fluid
ε_{ff}	energy parameter for fluid-fluid interaction which represents depth of the square-well potential
ε_{sf}	energy parameter for fluid-pore wall interaction which represents depth of the first well in the dual-square-well potential
θ	relative pore fluid density
λ	de Broglie wavelength
μ	chemical potential
ρ	total density in pore
$\rho_{\max}$	fluid close-packing density
σ	diameter of molecule
$\tau_{1\text{-}2}$	parameters in fraction functions under random distribution
ω	acentric factor

Subscripts

b	bulk-state fluid
co	core-region fluid
i, j	fluid component
rgn	abbreviation of region, which denotes the core region or the surface-adsorbed region
sf	surface-adsorbed-region fluid

Appendix A. Equation of state: chemical potential

Chemical potential (μ) is derived by Eq. (3) from Helmholtz free energy (A), Eq. (38). For a system with n_i moles of component i ($i = 1, 2, \ldots, NC$) and a total volume of V at temperature T, the partial derivative relations are (δ is the Kronecker delta function):

$$\frac{\partial x_j}{\partial n_i} = \frac{\delta_{ji}}{\sum_{k=1}^{NC} n_k} - \frac{n_j}{\left(\sum_{k=1}^{NC} n_k\right)^2} \tag{A.1}$$

$$\frac{\partial \theta}{\partial n_i} = -\frac{\theta b_{p,i}}{\sum_{k=1}^{NC} n_k b_{p,k}} \tag{A.2}$$

$$\frac{\partial F_{p2,j}}{\partial n_i} = \beta_{2,j}\gamma(\theta-1)^{\gamma-1}(1-F_{pr2,j})\left(1-\exp\left(-\frac{\beta_{0,j}}{T}\right)\right)\exp(-\beta_{2,j}(\theta-1)^{\gamma})\frac{\partial \theta}{\partial n_i} \tag{A.3}$$

$$\frac{\partial \overline{F}_{pr2}}{\partial n_i} = \sum_{k=1}^{NC} \frac{\partial x_k}{\partial n_i} F_{pr2,k} \tag{A.4}$$

For the core-region fluid, the total mole of fluid species is n_{co} and the partial derivative relations are:

$$n_{co} = \sum_{k=1}^{NC} n_{co,k} \tag{A.5}$$

$$\frac{\partial n_{co,j}}{\partial n_i} = (1-F_{p2,j})\delta_{ji} - n_j \frac{\partial F_{p2,j}}{\partial n_i} \tag{A.6}$$

$$\frac{\partial n_{co}}{\partial n_i} = \sum_{k=1}^{NC} \frac{\partial n_{co,k}}{\partial n_i} \tag{A.7}$$

$$\frac{\partial x_{co,j}}{\partial n_i} = -\frac{n_{co,j}}{n_{co}^2}\frac{\partial n_{co}}{\partial n_i} + \frac{1}{n_{co}}\frac{\partial n_{co,j}}{\partial n_i} \tag{A.8}$$

$$\frac{\partial a_{p,co}}{\partial n_l} = \sum_{i=1}^{NC}\sum_{j=1}^{NC}\left(\frac{\partial x_{co,i}}{\partial n_l}x_{co,j} + \frac{\partial x_{co,j}}{\partial n_l}x_{co,i}\right)\sqrt{a_i a_j}(1-k_{ij}) \tag{A.9}$$

$$\frac{\partial b_{p,co}}{\partial n_i} = \sum_{k=1}^{NC}\left(\frac{\partial x_{co,k}}{\partial n_i}b_{p,k}\right) \tag{A.10}$$

$$\frac{\partial v_{co}}{\partial n_i} = -\frac{V-V_{sf}}{n_{co}^2}\frac{\partial n_{co}}{\partial n_i} - \frac{V}{n_{co}}\frac{\partial \overline{F}_{pr2}}{\partial n_i} \tag{A.11}$$

Similarly, for the surface adsorbed region fluid:

$$n_{sf} = \sum_{k=1}^{NC} n_{sf,k} \tag{A.12}$$

$$\frac{\partial n_{sf,j}}{\partial n_i} = F_{p2,j}\delta_{ji} + n_j\frac{\partial F_{p2,j}}{\partial n_i} \tag{A.13}$$

$$\frac{\partial n_{sf}}{\partial n_i} = \sum_{k=1}^{NC}\frac{\partial n_{sf,k}}{\partial n_i} \tag{A.14}$$

$$\frac{\partial x_{sf,j}}{\partial n_i} = -\frac{n_{sf,j}}{n_{sf}^2}\frac{\partial n_{sf}}{\partial n_i} + \frac{1}{n_{sf}}\frac{\partial n_{sf,j}}{\partial n_i} \tag{A.15}$$

$$\frac{\partial a_{p,sf}}{\partial n_l} = \sum_{i=1}^{NC}\sum_{j=1}^{NC}\left(\frac{\partial x_{sf,i}}{\partial n_l}x_{sf,j} + \frac{\partial x_{sf,j}}{\partial n_l}x_{sf,i}\right)\sqrt{a_i a_j}(1-k_{ij})h_{sf} \tag{A.16}$$

$$\frac{\partial b_{p,sf}}{\partial n_i} = \sum_{k=1}^{NC}\left(\frac{\partial x_{sf,k}}{\partial n_i}b_{p,k}\right) \tag{A.17}$$

$$\frac{\partial v_{sf}}{\partial n_i} = -\frac{V_{sf}}{n_{sf}^2}\frac{\partial n_{sf}}{\partial n_i} + \frac{V}{n_{sf}}\frac{\partial \overline{F}_{pr2}}{\partial n_i} \tag{A.18}$$

Next, the chemical potential of component i derived by Eq. (3) is:

$$\mu_i = \mu_{0,i} - RT + \sum_{rgn=co,sf}\sum_{k=1}^{NC}\left(\frac{\partial n_{rgn,k}}{\partial n_i}RT\ln\left(\frac{N_{av}x_{rgn,k}\lambda_k^3}{v_{rgn}-b_{p,rgn}}\right) + n_{rgn}RT\frac{\partial x_{rgn,k}}{\partial n_i}\right.$$
$$\left.-\frac{n_{rgn,k}RT}{v_{rgn}-b_{p,rgn}}\left(\frac{\partial v_{rgn}}{\partial n_i}-\frac{\partial b_{p,rgn}}{\partial n_i}\right)\right)$$
$$-\sum_{rgn=co,sf}\left(\frac{n_{rgn}a_{p,rgn}}{b_{p,rgn}}\cdot\frac{v_{rgn}\frac{\partial b_{p,rgn}}{\partial n_i}-\frac{\partial v_{rgn}}{\partial n_i}b_{p,rgn}}{v_{rgn}^2+2v_{rgn}b_{p,rgn}-b_{p,rgn}^2}\right.$$
$$+\frac{\sqrt{2}}{4}\ln\left(\frac{v_{rgn}+\left(1+\sqrt{2}\right)b_{p,rgn}}{v_{rgn}+\left(1-\sqrt{2}\right)b_{p,rgn}}\right)\left(\frac{a_{p,rgn}}{b_{p,rgn}}\frac{\partial n_{rgn}}{\partial n_i}+\frac{n_{rgn}}{b_{p,rgn}}\frac{\partial a_{p,rgn}}{\partial n_i}\right.$$
$$\left.\left.-\frac{n_{rgn}a_{p,rgn}}{b_{p,rgn}^2}\frac{\partial b_{p,rgn}}{\partial n_i}\right)\right)$$
$$-\frac{3}{4}N_{av}\varepsilon_{sf,i}\left(F_{pr1,i}\right.$$
$$\left.+\left(1-F_{pr1,i}\right)\left(1-\frac{T}{\beta_{0,i}}\left(1-\exp\left(-\frac{\beta_{0,i}}{T}\right)\right)\right)\left(1-\exp\left(-\beta_{1,i}(\theta-1)^{\gamma}\right)\right)\right)$$
$$-\sum_{k=1}^{NC}\frac{3}{4}N_{av}n_k\varepsilon_{sf,k}\beta_{1,k}\gamma(\theta-1)^{\gamma-1}\frac{\partial\theta}{\partial n_i}\left(1-F_{pr1,k}\right)\left(1\right.$$
$$\left.1-\frac{T}{\beta_{0,k}}\left(1-\exp\left(-\frac{\beta_{0,k}}{T}\right)\right)\right)\exp\left(-\beta_{1,k}(\theta-1)^{\gamma}\right)$$
$$-\frac{1}{4}N_{av}\varepsilon_{sf,i}\left(F_{pr2,i}\right.$$
$$\left.+\left(1-F_{pr2,i}\right)\left(1-\frac{T}{\beta_{0,i}}\left(1-\exp\left(-\frac{\beta_{0,i}}{T}\right)\right)\right)\left(1-\exp\left(-\beta_{2,i}(\theta-1)^{\gamma}\right)\right)\right)$$
$$-\sum_{k=1}^{NC}\frac{1}{4}N_{av}n_k\varepsilon_{sf,k}\beta_{2,k}\gamma(\theta-1)^{\gamma-1}\frac{\partial\theta}{\partial n_i}\left(1-F_{pr2,k}\right)\left(1\right.$$
$$\left.-\frac{T}{\beta_{0,k}}\left(1-\exp\left(-\frac{\beta_{0,k}}{T}\right)\right)\right)\exp\left(-\beta_{2,k}(\theta-1)^{\gamma}\right) \quad (A.19)$$

References

[1] D. Fairén-Jiménez, F. Carrasco-Marín, C. Moreno-Castilla, Adsorption of benzene, toluene, and xylenes on monolithic carbon aerogels from dry air flows, Langmuir 23 (2007) 10095–10101.

[2] A. Angelova, B. Angelov, S. Lesieur, R. Mutafchieva, M. Ollivon, C. Bourgaux, R. Willumeit, P. Couvreur, Dynamic control of nanofluidic channels in protein drug delivery vehicles, J. Drug Deliv. Sci. Technol. 18 (2008) 41–45.

[3] A. Corma, M.T. Navarro, J.P. Pariente, Synthesis of an ultralarge pore titanium silicate isomorphous to MCM-41 and its application as a catalyst for selective oxidation of hydrocarbons, J. Chem. Soc., Chem. Commun. (1994) 147–148.

[4] F. Civan, D. Devegowda, R. Sigal, Theoretical fundamentals, critical issues, and adequate formulation of effective shale gas and condensate reservoir simulation, AIP Conference Proceedings 1453 (2012) 155–160.

[5] S. Wang, Q. Feng, F. Javadpour, T. Xia, Z. Li, Oil adsorption in shale nanopores and its effect on recoverable oil-in-place, Int. J. Coal Geol. 147–148 (2015) 9–24.

[6] M. Thommes, R. Köhn, M. Fröba, Sorption and pore condensation behavior of pure fluids in mesoporous MCM-48 silica, MCM-41 silica, SBA-15 silica and controlled-pore glass at temperatures above and below the bulk triple point, Appl. Surf. Sci. 196 (2002) 239–249.

[7] H.Y. Zhu, L.A. Ni, G.Q. Lu, A pore-size-dependent equation of state for multilayer adsorption in cylindrical mesopores, Langmuir 15 (1999) 3632–3641.

[8] D. Cao, W. Wang, Z. Shen, J. Chen, Determination of pore size distribution and adsorption of methane and CCl4 on activated carbon by molecular simulation, Carbon 40 (2002) 2359–2365.

[9] P. Trens, N. Tanchoux, P.-M. Papineschi, D. Maldonado, F. di Renzo, F. Fajula, Confinements effects in MCM-41-type materials: comparison of the energetics of n-hexane and 1-hexene adsorption, Microporous Mesoporous Mater. 86 (2005) 354–363.

[10] S. Luo, J.L. Lutkenhaus, H. Nasrabadi, Experimental study of confinement effect on hydrocarbon phase behavior in nano-scale porous media using differential scanning calorimetry, in: SPE Annual Technical Conference and Exhibition, Society of Petroleum Engineers, Houston, Texas, USA, 2015. SPE-175095-MS.

[11] S. Luo, J.L. Lutkenhaus, H. Nasrabadi, Confinement-induced supercriticality and phase equilibria of hydrocarbons in nanopores, Langmuir 32 (2016) 11506–11513.

[12] S. Luo, J.L. Lutkenhaus, H. Nasrabadi, Multi-scale fluid phase behavior simulation in shale reservoirs by a pore-size-dependent equation of state, in: SPE Annual Technical Conference and Exhibition, Society of Petroleum Engineers, San Antonio, Texas, USA, 2017. SPE-187422-MS.

[13] J.P.R.B. Walton, N. Quirke, Capillary condensation: a molecular simulation study, Mol. Simul. 2 (1989) 361–391.

[14] B. Jin, R. Bi, H. Nasrabadi, Molecular simulation of the pore size distribution effect on phase behavior of methane confined in nanopores, Fluid Phase Equilib. 452 (2017) 94–102.

[15] B. Jin, H. Nasrabadi, Phase behavior of multi-component hydrocarbon systems in nano-pores using gauge-GCMC molecular simulation, Fluid Phase Equilib.

425 (2016) 324–334.
[16] B. Jin, H. Nasrabadi, Phase Behavior in Shale Organic/Inorganic Nanopores from Molecular Simulation, SPE Reservoir Evaluation & Engineering, preprint, 2018.
[17] Z. Li, Z. Jin, A. Firoozabadi, Phase behavior and adsorption of pure substances and mixtures and characterization in nanopore structures by density functional theory, SPE J. 19 (2014). SPE-169819-PA.
[18] Z. Jin, A. Firoozabadi, Thermodynamic modeling of phase behavior in shale media, SPE J. 21 (2016) 190–207. SPE-176015-PA.
[19] Z. Li, D. Cao, J. Wu, Layering, condensation, and evaporation of short chains in narrow slit pores, J. Chem. Phys. 122 (2005) 224701.
[20] X. Zhang, W. Wang, Square-well fluids in confined space with discretely attractive wall-fluid potentials: critical point shift, Phys. Rev. 74 (2006) 062601.
[21] X. Zhang, D. Cao, W. Wang, The effect of discrete attractive fluid–wall interaction potentials on adsorption isotherms of Lennard-Jones fluid in cylindrical pores, J. Chem. Phys. 119 (2003) 12586–12592.
[22] D.-Y. Peng, D.B. Robinson, A new two-constant equation of state, Ind. Eng. Chem. Fundam. 15 (1976) 59–64.
[23] J.S. Lopez-Echeverry, S. Reif-Acherman, E. Araujo-Lopez, Peng-Robinson equation of state: 40 years through cubics, Fluid Phase Equilib. 447 (2017) 39–71.
[24] B. Nojabaei, R.T. Johns, L. Chu, Effect of capillary pressure on phase behavior in tight rocks and shales, SPE J. 16 (2013) 281–289. SPE-159258-PA.
[25] N.S. Alharthy, T. Nguyen, H. Kazemi, T. Teklu, R. Graves, Multiphase compositional modeling in small-scale pores of unconventional shale reservoirs, in: SPE Annual Technical Conference and Exhibition, Society of Petroleum Engineers, New Orleans, Louisiana, USA, 2013. SPE-166306-MS.
[26] X. Dong, H. Liu, J. Hou, K. Wu, Z. Chen, Phase equilibria of confined fluids in nanopores of tight and shale rocks considering the effect of capillary pressure and adsorption film, Ind. Eng. Chem. Res. 55 (2016) 798–811.
[27] Y. Zhang, W. Yu, K. Sepehrnoori, Y. Di, Investigation of nanopore confinement on fluid flow in tight reservoirs, J. Pet. Sci. Eng. 150 (2017) 265–271.
[28] S.P. Tan, M. Piri, Equation-of-state modeling of associating-fluids phase equilibria in nanopores, Fluid Phase Equilib. 405 (2015) 157–166.
[29] S.P. Tan, M. Piri, Equation-of-state modeling of confined-fluid phase equilibria in nanopores, Fluid Phase Equilib. 393 (2015) 48–63.
[30] L. Travalloni, M. Castier, F.W. Tavares, S.I. Sandler, Thermodynamic modeling of confined fluids using an extension of the generalized van der Waals theory, Chem. Eng. Sci. 65 (2010) 3088–3099.
[31] L. Travalloni, M. Castier, F.W. Tavares, Phase equilibrium of fluids confined in porous media from an extended Peng–Robinson equation of state, Fluid Phase Equilib. 362 (2014) 335–341.
[32] G.D. Barbosa, L. Travalloni, M. Castier, F.W. Tavares, Extending an equation of state to confined fluids with basis on molecular simulations, Chem. Eng. Sci. 153 (2016) 212–220.
[33] G.D. Barbosa, M.L. D'Lima, S.M.H. Daghash, M. Castier, F.W. Tavares, L. Travalloni, Cubic equations of state extended to confined fluids: new mixing rules and extension to spherical pores, Chem. Eng. Sci. 184 (2018) 52–61.
[34] X. Dong, H. Liu, W. Guo, J. Hou, Z. Chen, K. Wu, Study of the confined behavior of hydrocarbons in organic nanopores by the potential theory, Fluid Phase Equilib. 429 (2016) 214–226.
[35] N. Dawass, M.L. D'Lima, I.G. Economou, M. Castier, Phase equilibrium with external fields: application to confined fluids, J. Chem. Eng. Data 61 (2016) 2873–2885.
[36] L. Travalloni, M. Castier, F.W. Tavares, S.I. Sandler, Critical behavior of pure confined fluids from an extension of the van der Waals equation of state, J. Supercrit. Fluids 55 (2010) 455–461.
[37] A. Wongkoblap, D.D. Do, G. Birkett, D. Nicholson, A critical assessment of capillary condensation and evaporation equations: a computer simulation study, J. Colloid Interface Sci. 356 (2011) 672–680.
[38] T.L. Hill, An Introduction to Statistical Thermodynamics, Courier Corporation, 1986.
[39] S. Luo, H. Nasrabadi, J.L. Lutkenhaus, Effect of confinement on the bubble points of hydrocarbons in nanoporous media, AIChE J. 62 (2016) 1772–1780.
[40] X. Zhang, D. Cao, W. Wang, A stepwise approximation for modeling of the wall–fluid potential of a mesoscopic pore, J. Colloid Interface Sci. 308 (2007) 49–52.
[41] S.I. Sandler, An Introduction to Applied Statistical Thermodynamics, John Wiley & Sons, 2010.
[42] S.I. Sandler, From molecular theory to thermodynamic models: Part I. Pure fluids, Chem. Eng. Educ. 24 (1990) 12–19.
[43] P.M. Mathias, T. Naheiri, E.M. Oh, A density correction for the Peng—robinson equation of state, Fluid Phase Equilib. 47 (1989) 77–87.
[44] R. Evans, U.M.B. Marconi, P. Tarazona, Fluids in narrow pores: adsorption, capillary condensation, and critical points, J. Chem. Phys. 84 (1986) 2376–2399.
[45] P.A. Monson, Understanding adsorption/desorption hysteresis for fluids in mesoporous materials using simple molecular models and classical density functional theory, Microporous Mesoporous Mater. 160 (2012) 47–66.
[46] C. Fan, Y. Zeng, D.D. Do, D. Nicholson, An undulation theory for condensation in open end slit pores: critical hysteresis temperature & critical hysteresis pore size, Phys. Chem. Chem. Phys. 16 (2014) 12362–12373.
[47] C.G. Sonwane, S.K. Bhatia, N. Calos, Experimental and theoretical investigations of adsorption hysteresis and criticality in MCM-41: studies with O2, Ar, and CO2, Ind. Eng. Chem. Res. 37 (1998) 2271–2283.
[48] P.H. Emmett, M. Cines, Adsorption of argon, nitrogen, and butane on porous glass, J. Phys. Colloid Chem. 51 (1947) 1248–1262.
[49] H. Tanaka, T. Hiratsuka, N. Nishiyama, K. Mori, M. Miyahara, Capillary condensation in mesoporous silica with surface roughness, Adsorption 19 (2013) 631–641.
[50] M. Thommes, G.H. Findenegg, Pore condensation and critical-point shift of a fluid in controlled-pore glass, Langmuir 10 (1994) 4270–4277.
[51] J.-H. Yun, T. Düren, F.J. Keil, N.A. Seaton, Adsorption of methane, ethane, and their binary mixtures on MCM-41: experimental evaluation of methods for the prediction of adsorption equilibrium, Langmuir 18 (2002) 2693–2701.
[52] M.A.O. Lourenço, C. Siquet, M. Sardo, L. Mafra, J. Pires, M. Jorge, M.L. Pinto, P. Ferreira, J.R.B. Gomes, Interaction of CO2 and CH4 with functionalized periodic mesoporous phenylene–silica: periodic DFT calculations and gas adsorption measurements, J. Phys. Chem. C 120 (2016) 3863–3875.
[53] Y. He, N.A. Seaton, Experimental and computer simulation studies of the adsorption of ethane, carbon dioxide, and their binary mixtures in MCM-41, Langmuir 19 (2003) 10132–10138.
[54] M.A. Ioneva, R.G. Mallinson, J.H. Harwell, Capillary condensation of light hydrocarbons in MCM-41 - type mesoporous materials, MRS Proceedings 454 (2011) 119.
[55] P.A. Russo, M.M.L.R. Carrott, P.J.M. Carrott, Hydrocarbons adsorption on templated mesoporous materials: effect of the pore size, geometry and surface chemistry, New J. Chem. 35 (2011) 407–416.
[56] S.Z. Qiao, S.K. Bhatia, D. Nicholson, Study of hexane adsorption in nanoporous MCM-41 silica, Langmuir 20 (2004) 389–395.
[57] M.M.L. Ribeiro Carrott, A.J.E. Candeias, P.J.M. Carrott, P.I. Ravikovitch, A.V. Neimark, A.D. Sequeira, Adsorption of nitrogen, neopentane, n-hexane, benzene and methanol for the evaluation of pore sizes in silica grades of MCM-41, Microporous Mesoporous Mater. 47 (2001) 323–337.
[58] S.K. Singh, J.K. Singh, Effect of pore morphology on vapor–liquid phase transition and crossover behavior of critical properties from 3D to 2D, Fluid Phase Equilib. 300 (2011) 182–187.
[59] K. Kuraoka, Y. Chujo, T. Yazawa, Hydrocarbon separation via porous glass membranes surface-modified using organosilane compounds, J. Membr. Sci. 182 (2001) 139–149.
[60] T. Monde, N. Nakayama, K. Yano, T. Yoko, T. Konakahara, Adsorption characteristics of silica gels treated with fluorinated silylation agents, J. Colloid Interface Sci. 185 (1997) 111–118.